Journal of Nanobiotechnology

RESEARCH

Open Access

NIR-II light based combinatorial management of hypertrophic scar by inducing autophagy in fibroblasts

Yunxian Dong[1,2†], Haibin Wang[1†], Youliang Zhang[1†], Yanqun Wu[1], Ling Lu[4], Hao Yu[1], Lingcong Zhou[1], Peng Zhao[4], Sixue Ouyang[5], Zibin Song[6], Zhicheng Hu[3], Dongming Lv[3], Yanchao Rong[3], Zirui Zhao[3], Jia Tao[5*], Bing Tang[3*] and Shengkang Luo[1*]

Abstract

The hypertrophic scar (HS) is a prevalent cutaneous fibrotic disorder that impacts both the aesthetic and functional aspects of the skin, there is an urgent need for a highly safe and effective approach to address the challenge of HS with thick and deep types. Inspired by the superior deep tissue penetrative ability of near-infrared-II (NIR-II) light and potential mitochondria ROS inducing effect of Chinese medicine lycorine (LYC), we fabricated a Cu_2Se@LYC (CL) composite by encapsulating LYC on polyvinyl pyrrolidone (PVP) modified Cu_2Se nanoparticles. After NIR-II irradiation, CL could induce the generation of reactive oxygen species (ROS) and mitochondrial damage in hypertrophic scar fibroblasts (HSFs). The subsequent release of cytochrome C (cyt-c) from mitochondria into the cytoplasm and upregulation of beclin1 leads to the activation of endogenous apoptosis and autophagy-mediated cell death. The CL + NIR-II treatment exhibited a pronounced anti-scarring effect in both in vitro and in vivo rabbit ear scar models, leading to a significant reduction in the fibrotic markers including Collagen I/III and α-smooth muscle actin (α-SMA). This study comprehensively investigated the crucial role of HSFs' autophagy in scar management and proposed a safe and effective therapy based on NIR-II laser for clinical application.

Keywords Hypertrophic scar, Autophagy, Photothermal therapy, Lycorine, Apoptosis

†Yunxian Dong, Haibin Wang and Youliang Zhang contributed equally to this work.

*Correspondence:
Jia Tao
cejtao@scut.edu.cn
Bing Tang
tangbing@mail.sysu.edu.cn
Shengkang Luo
luoshk@gd2h.org.cn
[1]Department of Plastic and Reconstructive Surgery, Guangdong Second Provincial General Hospital, No.466 Middle Xin Gang Road, Guangzhou 510317, China
[2]Department of Plastic and Cosmetic Surgery, Nanfang Hospital, Southern Medical University, Guangzhou, China
[3]Department of Burns, Wound Repair and Reconstruction, the First Affiliated Hospital of Sun Yat-sen University, No.58 Zhongshan Er Road, Guangzhou 510080, China
[4]NMPA Key Laboratory for Research and Evaluation of Drug Metabolism, Guangdong Provincial Key Laboratory of New Drug Screening, Guangdong Provincial Key Laboratory of Cardiac Function and Microcirculation, School of Pharmaceutical Sciences, Southern Medical University, Guangzhou, China
[5]School of Chemistry and Chemical Engineering, South China University of Technology, No. 381 Wushan Road, Guangzhou 510640, China
[6]Institute of Brain Diseases, Department of Neurosurgery, Southern Medical University Nanfang Hospital, Guangzhou, China

Introduction

Hypertrophic scar (HS) is a common skin fibrotic disease, occurring in various acute or chronic wounds, deep burns and incisions after various surgical operations [1]. The overall incidence rate of HS ranges from 4 to 16%, while the prevalence after injury in burn patients is as high as 70%.[2] HS not only impacts the patient's appearance but also leads to impaired skin function, joint deformities, and even activity disorders, thereby exerting a dual serious influence on mental and physical well-being [3]. Therefore, the treatment of hypertrophic scars holds immense significance, especially for deep and thick types.

Current therapeutic approaches for HSs encompass both surgical and non-surgical modalities, including surgical excision, silicone-based medications, laser treatments, corticosteroid hormone injections and etc [4, 5]. Laser therapy is highly favored by patients due to its non-invasive approach and shorter treatment duration, making it a widely utilized modality in clinical settings [6]. However, the effectiveness and applicability of laser therapy are limited by multiple reasons [7]. For example, the limited depth of penetration restricts the Er: YAG laser's impact to the epidermal layer, rendering it more suitable for addressing superficial scars rather than HS characterized by greater thickness [8, 9]. CO_2 fractional laser causes more substantial thermal damage to the skin and is associated with increased pain during treatment along with a higher likelihood of postoperative erythema and pigmentation issues [9, 10]. In view of the larger thickness of HSs, laser therapy still offers significant rooms for advancement and refinement.

In normal physiological state, after skin dermal tissue injury, it undergoes an initial stage of bleeding and coagulation reaction, followed by an inflammatory reaction stage [11–13]. The proliferation period commences approximately one week post-injury, facilitating subsequent tissue maturation and remodeling [11]. The pathogenesis of hypertrophic scars primarily involves the persistent proliferation of fibroblasts in the dermis and excessive deposition of extracellular matrix (ECM) [1, 14]. Pathologically, in response to cytokine stimulation such as TGF-β, fibroblasts exhibit sustained secretion of elevated levels of collagen (primarily type I and III) and alpha smooth muscle actin (α-SMA), leading to a phenotypic transition into myofibroblasts and subsequent formation of hypertrophic scars [15]. The deposition of collagen in the ECM can lead to the stiffening of scar tissue, while α-SMA can enhance fibroblasts' contractile ability, resulting in scar contracture and skin traction [16, 17]. The targeted reduction of fibroblast proliferation and promotion of cell death represent a promising therapeutic strategy for the treatment of HS [18, 19].

Autophagy, serving as a pathway for the cyclic degradation of intracellular proteins and damaged organelles, plays a pivotal role in maintaining cellular homeostasis [20]. The autophagosome, characterized by its double membrane structure, engulfs cellular "waste" and transports it to the lysosome for degradation and subsequent recycling within the cell [21–23]. Nevertheless, mounting evidence suggests that over-activated autophagy may result in mitochondrial damage, depletion of metabolic energy, and eventual cell death [24]. The processes of autophagy and apoptosis, although classified as distinct forms of programmed cell death (PCD), are intricately interconnected and regulated by shared factors such as autophagy regulatory factor beclin 1, apoptosis inhibitor Bcl 2, calmodulin-dependent protein kinases, AKT/mTOR signaling pathway [25–28]. Targeting autophagy is also a promising therapeutic strategy for the treatment of hypertrophic scars [29, 30]. Enhancing autophagy through inhibition of PI3K/AKT/mTOR signaling pathways has been demonstrated to effectively mitigate the formation of HSs [20]. 5-aminolevulinic acid-based photodynamic therapy could induce autophagic cell death in keloid fibroblasts through the SIRT1/SIRT3/SOD2/mROS pathway [31]. Although both HSs and keloids are fibrotic skin diseases, they exhibit distinct pathological characteristics: HSs remain within the boundaries of the original injury area, whereas keloids display tumor-like growth patterns [1]. Given the high prevalence of HSs and their propensity to cause joint contracture deformities, our focus primarily revolves around investigating HS [16].

Herein, this study investigated the activation of apoptosis and autophagy to regulate the biological behavior and fibrosis of hypertrophic scar fibroblasts (HSFs), which was realized through the synergistic treatment of near-infrared region II (NIR-II) laser illumination and Cu_2Se@LYC (CL) nanoparticles (NPs) [32, 33]. The CL NPs were synthesized by incorporating lycorine onto polyvinyl pyrrolidone (PVP) coated Cu_2Se NPs (Scheme. 1 A). Lycorine is a Chinese medicine with potential mitochondria ROS inducing effects, and Cu_2Se NPs is an effective near-infrared-II (NIR-II, 1064 nm) photothermal conversion agent [34]. The present results indicated that the NIR-II photothermal effect of Cu_2Se in CL remained effective for simulated scar with a thickness of 10 mm. The NIR-II laser illumination and CL collectively induce endogenous apoptosis and autophagic cell death in HSFs (Scheme1. B). Moreover, an in vivo rabbit ear scar model was established, the CL+NIR-II based treatment can effectively reduce the scar elevation index (SEI) from 3.87 to 1.67 through enhancing autophagy and alleviating fibrosis.

Materials and methods

Preparation of Cu2Se@LYC

Step 1: 0.2 g of PVP (Macklin, Shanghai, China) was added to a 50 mL glass beaker, followed by the addition

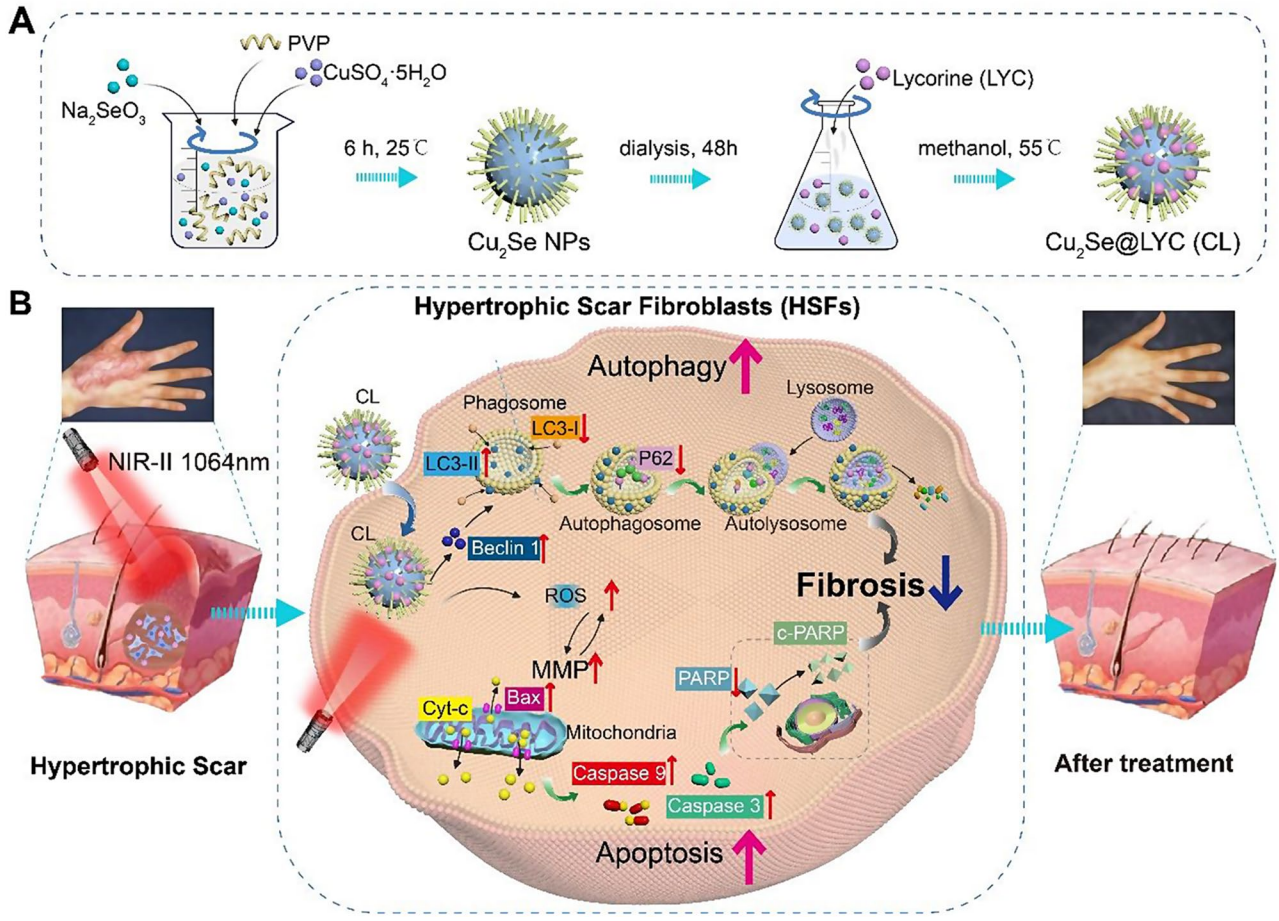

Scheme 1 Scheme1 Schematic of Cu_2Se@LYC NPs (CL) combined with NIR-II (1064 nm) phototherapy for hypertrophic scar (HS). (A) Process of CL preparation. (B)The NIR-II laser illumination and CL collectively induce endogenous apoptosis and autophagic cell death in hypertrophic scar fibroblasts (HSFs).

of 20 mL deionized water for dissolution. Subsequently, introduce Na_2SeO_3 (0.2 mmol, Macklin, Shanghai, China) and vitamin C (VC, 0.4 mmol) into the aforementioned solution and agitate at room temperature for a duration of 30 min. During this period, the solution will undergo a transformation, exhibiting a vibrant red hue. At this time, the solution will turn red. Then, the addition of $CuSO_4 \cdot 5H_2O$ (0.1 mmol, Macklin, Shanghai, China) and VC (5 mmol) to another prepared beaker was followed by the addition of 10 mL deionized water for rapid dissolution, resulting in the formation of a homogeneous milky mixture. Step 2: Mix the solutions obtained in step 1 and step 2, followed by stirring at ambient temperature for a duration of 6 h to ensure complete reaction. Then, the black Cu_2Se NPs solution was obtained. The Cu_2Se solution was ultimately transferred to a dialysis bag (MWCO 3.5 kDa), subjected to purification via dialysis in 2 L deionized water for 2 days, and subsequently stored at 4 °C. Cu_2Se NPs is obtained after step 1–3. Step 3: CL NPs is synthesized from Cu_2Se NPs and LYC (Glpbio, Montclair, USA). Specifically, the freeze-dried Cu_2Se NPs were dissolved in methanol (Macklin, Shanghai, China) and subjected to ultrasonic shock for 15 min. Then LYC was added and the reaction mixture was stirred at 55℃ until the methanol completely evaporated.

Characterization of Cu2Se@LYC

The surface morphology, elemental distribution and energy dispersive spectroscopy (EDS) mapping composition of Cu_2Se were analyzed using high-resolution transmission electron microscopy (HRTEM, JEM-2100 F, JEOL, Japan) in combination with X-ray energy spectrometer (XFlash-5030T, Bruker, Germany). The X-ray photoelectron spectroscopy (XPS) was measured by X-ray photoelectron spectrometer (ESCALAB-250Xi, Thermo, USA). The Fourier transform infrared (FT-IR) spectra was obtained using an infrared spectrometer (Nicolet-6700, Thermo, USA). Ultraviolet-visible-near-infrared spectra of NPs were measured by spectrophotometer (PerkinElmer Lambda 750, USA).

The PTT effect of Cu2Se@LYC

First, the same laser intensity of 1064 nm (1 W/cm^2) was employed to irradiate deionized water and Cu_2Se NPs

solution with varying concentrations (10, 25, 50, 100 μg/mL) for 5 min in order to assess their photothermal properties. Subsequently, different laser intensity (0.5, 0.75, 1.0, 1.5 W/cm^2) were investigated at a constant concentration of Cu_2Se (50 μg/mL). The photothermal stability of Cu_2Se NPs was evaluated through five cycles of laser on/off switching. The temperature variations and thermal images during the treatments were monitored using an infrared thermal imager (Fortric 225). The photothermal conversion efficiency was calculated according to the studies reported.

Cell culture

This study was approved by the Ethics Committee for Clinical Research and Animal Trials of Guangdong Second Provincial General Hospital (Guangzhou, China, approval number: 2023-DW-KZ-034), and written informed consent was obtained from all participants. It follows the requirements of the Declaration of Helsinki. Skin scar tissues were performed on 10 patients with HS, including 5 females and 5 males aged between 18 and 39 years (mean 25.8±6.43 years), after obtaining informed consent, the details are shown in additional fle: Table S1. The criteria for inclusion and exclusion: these HS patients were newly diagnosed and untreated, as confirmed by histological analysis. Skin fibroblasts were isolated and cultured following the methodology described in our previous study [18, 20]. In brief, individual skin tissues were cut into small pieces measuring 1 mm [3] and then digested using type II collagenase (Yuanye, Shanghai, China) at a temperature of 37 °C for a duration of 8 h. HSFs were cultured in 1×DMEM medium (Gibco, New York, USA) supplemented with fetal bovine serum FBS (Gibco, New York, USA) at a concentration of 10%, maintaining the cells at a temperature of 37℃ under an atmosphere containing CO_2 levels of approximately 5%. Subsequent experiments utilized fibroblast cells from generations ranging between 3 and 6.

HaCaT cells were cultured in RPMI 1640 medium (GIBCO, Grand Island, NY) replenished with 10% fetal bovine serum (FBS; GIBCO) and 1% Pen/Step (GIBCO) at 37 °C in an atmosphere of 5% CO_2.

Cellular uptake ability of CL

HSFs were seeded in a confocal glass bottom dish (10 mm) at a density of 2000 cells and cultured for 24 h. After the HSFs incubated with Rhodamine B (Macklin, Shanghai, China)-conjugated CL for 2, 4 and 6 h, the cells were fixed with 4% paraformaldehyde (Solarbi, Beijing, China), sequentially stained with 4,6-diamidino-2-phenyiindole 2 hci (DAPI, keyGEN Nanjing, China), and finally observed with a confocal laser scanning microscopy (CLSM, LSM880 Basic Operation, Zeiss).

Cell cytotoxicity assay

HSFs (2×10^3 cells/well) were cultured in 96-well plates overnight and treated in triplicate with different doses of Cu_2Se and CL (0, 2.5, 5, 10, 20, and 40 μg/mL). After culturing for 6 h, the laser treatment group was irradiated using 1064 nm laser (1 W/cm^2, 5 min). After incubating the culture for 12–24 h, cell viability was determined using a Cell Counting Kit-8 (CCK8, Fudebio, Hangzhou, China), per the manufacturer's protocol.

Cell live-dead assay

HSFs were cultured in 6-well plates and when they reached 90% confluence, Cu_2Se and CL were added. After 6 h of culture, the laser treatment group was irradiated with 1064 nm laser (1 W/cm^2, 5 min). After incubation for another 1 h, cells were washed 3 times with PBS, then incubated with calflavonin AM/ propyl iodide (PI, keyGEN, Nanjing, China) for 30 min, and observed under fluorescence microscope.

Flow cytometry analysis

HSFs and NFs were plated in 6-well plates and cultured overnight. Cu_2Se and CL was added to the final concentrations of 20 μg/mL in each well and cells were incubated in incubator for 6 h. Then, NIR-II groups were irradiated with 1064 nm laser (1 W/cm^2, 5 min). The HSFs were cultured at 37℃ for another 24 h. After washing, they were incubated with 10 μM of 2,7-dichlorofluorescein (DCFH-DA, Elabscience, Wuhan, China) and cultured in the dark at 37℃ for 30 min. The cells were harvested for flow cytometry analysis of ROS in a Beckman Cyan flow cytometer (Beckman Coulter, Brea, CA, USA).

For the detection of apoptosis, the cells were harvested and stained with Annexin V-FITC and propidium iodide (PI, Elabscience, Wuhan, China) in the dark. Subsequently, the stained cells were subjected to examination using flow cytometer.

TUNEL assay

HSFs were seeded in confocal glass bottom dish for 24 h. Then the culture medium containing Cu_2Se or CL was subsequently replaced and maintained for 6 h, with or without 1064 nm laser irradiation. The TUNEL reaction was conducted after a 24-hour incubation. The cells were subjected to protease K treatment at 37 °C for 10 min, followed by cytomembrane disruption using 0.25% Triton-×100 (Solarbi, Beijing, China). Subsequently, the TDT enzyme, dUTP, and buffer were combined in a ratio of 1:5:50 as per the instructions provided with the tunel kit (Elabscience, Wuhan, China), and added to the dish to cover cells. The cell mixture was incubated at 37℃ for 1 h. Following a 15-minute DAPI staining protocol, the fluorescent signals (488 nm for green) were captured under a confocal microscopy (LSM880 Basic Operation,

Zeiss). The objective of the fluorescence image was 10×. The nuclei stained by DAPI are blue under ultraviolet excitation, and the positive apoptotic nuclei are green.

For rabbit ear tissue, paraffin sections are deparaffinized and rehydrated. After the sections were slightly dried, an immunohistochemical pen was used to draw a circle around the tissue to prevent the liquid from flowing away. The tissue is covered by a drop of protease K working solution inside the circle, and then the membrane was broken with 0.1%triton. After equilibrium at room temperature, the reaction solution (TDT enzyme, dUTP, buffer mixed at 1:5:50) was added and incubated at 37℃ for 1 h. DAPI was then restained and observed under fluorescence microscope.

Western blot analysis

The cells were harvested, dissolved in a radioimmunoprecipitation assay (RIPA) buffer (Fudebio, Hangzhou, China) containing protease and phosphatase inhibitors as well as phenylmethylsulfonyl fluoride (PMSF, Fudebio, Hangzhou, China), and then centrifuged. The protein concentration was determined using the BCA protein assay kit (Fudebio, Hangzhou, China). Cell lysate samples (50 μg/lane) were separated by SDS-PAGE on a 7.5-12.5% gel and transferred onto polyvinylidene difluoride (PVDF) membranes (Roche, Mannheim, Germany). TBST (tris buffered saline containing 0.5% Tween 20) was blocked with 5% defatted dry milk for an hour before being incubated overnight at 4 °C with primary antibody. Conjugated secondary antibodies conjugated to horseradish peroxidase (HRP) (1:5000, Cell Signaling Technology, #3108, #7076) were used for detection purposes. Mitochondrial proteins were extracted from cells using cell mitochondrial isolation kit (Elabscience, Wuhan, China). The primary antibodies included anti-Bax (1:1000, CST, USA, #5023S), anti-Bcl-2 (1:1000, CST, USA, #15071S), anti-caspase 9 (1:1000, Proteintech, USA, 10380-1-AP), anti-caspase3 (1:1000, Proteintech, USA, 19677-1-AP), PARP (1:1000, Proteintech, USA, 13371-1-AP), c-PARP (1:1000, CST, USA, #5625), anti-Cyt-c (1:1000, Proteintech, USA, 10993-1-AP), anti-GAPDH (1:1000, 60004-1-Ig, 1:5000), anti-Cox-IV (1:1000, CST, USA, #4850), anti-Collagen I (1:1000, Proteintech, USA, 14695-1-AP), anti-Collagen III (1:1000, Proteintech, USA, 22734-1-AP), anti-α-SMA (1:1000, Proteintech, USA, 14395-1-AP).

Wound healing assay

HSFs was cultured, and when they reached 90% confluence, the monolayer cells were scratched with the pipette tips. After washing out the non-adherent cells with PBS, the remaining cells were cultured for 6 h in the presence of 20 μg/mL Cu_2Se or CL. Then, the laser treatment group was irradiated using 1064 nm laser (1 W/cm^2) for 5 min. 24 h later, The wound healing of cell monolayer in each well was photoimaged and the percent of wound healing was calculated using ImageJ software. The migration rate was calculated through the following method:

Migration rate = (1-Distance between the scratch margins at 24 h / Distance between the scratch margins at 0 h)×100%.

Transwell migration assay

The digestive cells were centrifuged and resuspended in a serum-free medium. A suspension of 200 μL cells (approximately 5000 cells) was added to the transwell chamber (without gel), followed by the addition of 600 μL of 20% FBS medium to the lower cavity of the 24-well plate. A final concentration of 20 μg/mL Cu_2Se or CL was added to each well, and after 6 h, laser irradiation (1 W/cm^2, 5 min) was either applied or not applied. On the next day, the transwell chamber was removed and any unmigrated cells were eliminated. Subsequently, the cells were fixed with 4% paraformaldehyde for a duration of 30 min and stained with a solution containing 0.1% crystal violet (XXX) for an additional period of 30 min. Finally, photographs and cell counts were taken under a microscope.

Detection of mitochondrial membrane potential (MMP)

HSFs were treated with Cu_2Se or CL (with or without NIR-II irradiation). After incubating the culture for 24 h, the cells were stained with JC-1 (Elabscience, Wuhan, China) for 15 min at 37℃ in the dark. After being washed, the cells were analyzed under a CLSM (LSM880 Basic Operation, Zeiss). The average fluorescence intensity was calculated using ImageJ software.

TEM observation of NPs, mitochondria and autophagosome

For cellular uptake, the HSFs are simply treated with CL for 6 h. For the structural observation of mitochondria and autophagosomes, the cells were treated with drugs for 6 h, irradiated with NIR-II for 5 min, and then continued to culture for 24 h. Then, cells were fixed with 2.5% glutaraldehyde at 4 ℃ for 4–6 h. The cells were washed, dehydrated and embedded, followed by cutting into ultra-thin Sect. (70 nm). Finally, the intracellular NPs, mitochondria or autophagosomes in individual cells were observed by TEM (HT7700; Hitachi, Tokyo, Japan). Similarly, rabbit ear scar tissues were cut into small pieces (2×1×1 mm) and fixed by 2.5% glutaraldehyde. The tissue Sect. (70 nm) were subjected to TEM using the similar protocol.

Immunofluorescence (IF) staining

HSFs were cultured in confocal glass bottom dish overnight. Next day, cells were treated with Cu_2Se or CL

for 6 h, and then, NIR-II groups were irradiated with 1064 nm laser for 5 min. The cells were fixed with 4% paraformaldehyde for 20 min, infiltrated with 0.25% Triton-×100 for 20 min, sealed with 0.5% goat serum (Solarbi, Beijing, China) at 37℃ for 1 h, and then incubated at 4℃ overnight with primary antibody. After being washed, the bound antibodies were reacted with fluorescent secondary antibodies at room temperature for 1 h and co-stained with DAPI for 15 min. The fluorescent signals were captured under a CLSM (LSM880 Basic Operation, Zeiss). Similarly, rabbit ear scar tissue Sect. (5 μm) were fixed in 4% paraformaldehyde and subjected to immunofluorescence. The primary antibodies included anti-LC3 (1:200, Medical and Biological Laboratories, PD014), anti-Collagen I (1:400, Proteintech, 14695-1-AP), anti-Collagen III (1:400, Proteintech, 22734-1-AP) and anti-α-SMA (1:400, Proteintech, 14395-1-AP) for cells; anti-Collagen I (1:200, Proteintech,67288-1-Ig) and anti-α-SMA (1:200, Proteintech, 67735-1-Ig) for tissue.

Collagen gel contraction assay

The HSFs (5×10^5 cells/mL, 2 mL) were combined with rat tail collagen (900 μL, 5 mg/Ml, Solarbi, Beijing, China) and 10×DMEM (100 μL) (pH≈7), and cultured in 24-well plates (1 mL/well) under different treatments. After incubation at 37℃ for 30–60 min, the collagen gel from each well was collected, and photographs were taken after 24 h. The change in gel area was then calculated.

Hemolysis test

Fresh blood was obtained from New Zealand Rabbits, and the red blood cells were acquired via centrifugation (1000 g/min, 10 min). After washing with PBS for three times, the red blood cells were incubated with different concentrations of CL (5, 10, 20 and 40 mg/mL). Deionized water and normal saline were selected as positive and negative groups, respectively. After incubation for 4 h, the solution was centrifuged at 1000 g for 10 min and the optical density at 567 nm (OD567nm) of the samples were measured.

Establishment of rabbit ear scar model

All animal experimental protocols were approved by the Animal Experimental Center of the Guangdong Second Provincial General Hospital (approval number: 2023-DW-KZ-034). Four adult, male New Zealand white rabbits (weighing 2.0–2.5 kg) were from Guangdong medical laboratory animal center and housed in animal research facility with a cycle of 12-h light/dark. Individual rabbits were anesthetized using 1% pentobarbital sodium (1 mg/kg body weight), and wounded for a 10 mm round full-thickness (perichondrium was preserved) on their ventral surface of each ear using an easy dermal puncher, then the base skin was separated from the cartilage and the perichondrium was preserved. Two weeks after modeling, the rabbit ear scar formed and the rabbits were given different treatments. The specific grouping and treatment were as follows: ① Control group received an equivalent amount of normal saline injection into the scar; ② Cu_2Se+NIR-II group underwent subcutaneous injection of Cu_2Se along with 5 min of weekly NIR-II laser irradiation (0.5 W/cm^2,1064 nm); (3) In the CL group, only intra-scar injection of CL was administered; ④ In the CL+NIL-II group, in addition to CL injection, NIR-II laser irradiation was applied. During the evaluation of the photothermal effect in vivo, the scars were irradiated under 1064 nm laser at a power density of 0.5 W/cm^2 for 6 min. Regional thermal imaging and temperature changes of rabbit ear scars were observed with the FLIR E50 camera. The wound healing process and scar formation were monitored longitudinally. At the end of treatment, the scar tissues were dissected for histology, immunofluorescence and TEM analyses.

Histology

The dissected ear tissues were fixed in 10% of formalin overnight and paraffin-embedded. The tissue paraffin Sect. (5 μm) were regularly stained with H&E, Masson's trichrome and sirius red staining. Hematoxylin-eosin (H&E) high definition constant dye kit, Masson Tri-Color dyeing solution, Picrosirius Red dye and Immunohistochemical kit were purchased from Servicebio (Wuhan, China). The stained tissue sections were photoimaged and observed under a light microscope (Digital pathology section scanner, KFBIO, China, KF-PRO-020-HI) or a polarized light microscope (Upright optical microscope, Nikon, Japan, Eclipse E100). The protocols of TUNEL and IF staining for rabbit ear tissue were detailed in the preceding section.

For immunohistochemistry (IHC), dewaxed and rehydrated sections were immersed in a citric acid antigen recovery buffer (Servicebio, Wuhan, China). Subsequently, the sections were incubated in 3% hydrogen peroxide solution (Servicebio, Wuhan, China) for 25 min to block endogenous peroxidase activity, followed by blocking antibodies with 3% goat serum for 30 min. The sections were then exposed to the primary antibody overnight at 4 °C. On the next day, after washing with PBS, the sections were treated with secondary antibody at room temperature for 60 min. DAB color developer (Servicebio, Wuhan, China) was utilized to visualize the antibody binding site, while hematoxylin was employed as a counterstain. The primary antibodies included anti-TGF-β1 (1:1000, Proteintech, 69012-1-Ig), anti-Collagen I (1:1000, Proteintech,67288-1-Ig), anti-Collagen III (1:1000, Proteintech, 68320-1-Ig), anti-MMP3(1:1000,

Proteintech, 66338-1-Ig), anti-α-SMA (1:200, Proteintech, 67735-1-Ig).

Statistical analysis

The data are expressed as mean ± SD. The difference between the two groups was analyzed by the unpaired t-test analysis and the difference among multiple groups was analyzed by one-way ANOVA and post hoc Bonferroni's correction using SPSS 24.0 software. A P-value of <0.05 was considered statistically significant.

Results and discussion

Characterizations of Cu2Se@LYC

The Cu_2Se@LYC were synthesized through two steps: first, polyvinylpyrrolidone (PVP), Na_2SeO_3, and $CuSO_4{\cdot}5H_2O$ served as the precursor materials to synthesize Cu_2Se NPs; second, LYC was modified on Cu_2Se through the intermolecular hydrogen bonds with PVP (Scheme 1. A, Additional fle: Fig. 1) [32]. As shown in Fig. 1A, elemental mapping showed that Cu and Se elements were evenly distributed in the Cu_2Se NPs. Transmission electron microscopy (TEM) image showed that Cu_2Se NPs were homogeneously dispersed and performed spherical morphology with an average diameter of 53.35 ± 5.23 nm (Fig. 1B). In the high-resolution transmission electron microscopy (HRTEM), the Cu_2Se NPs showed the lattice spacing of 0.32 nm (Fig. 1B, C, Additional fle: Fig. S2), which corresponded to the previous reports [32]. In addition, energy dispersive spectroscopy (EDS) mapping (Fig. 1D) also demonstrated the presence of Cu and Se elements, with contents of 24.4% and 13.4%, respectively. The hydrodynamic diameters of Cu_2Se and Cu_2Se@LYC (CL) were determined to be 80.91 ± nm and 90.25 ± nm, respectively (Fig. 1E). The zeta potential of Cu_2Se and CL was detected as -20.0 mV and −30.7 mV (Additional fle: Fig. S3). X-ray photoelectron spectroscopy (XPS) reveals the predominant valence states of Cu_2Se, as evidenced by distinctive peaks observed in the C1s, N1s, O1s, Cu 2p and Se 3d orbitals (Fig. 1F). The peaks of Cu 2p3/2 and Cu 2p1/2 are centered at 931.6 and 932.5 eV, respectively, indicating the presence of Cu^{2+} and Cu^{+} on the CL surface. The presence of the Cu^{2+}

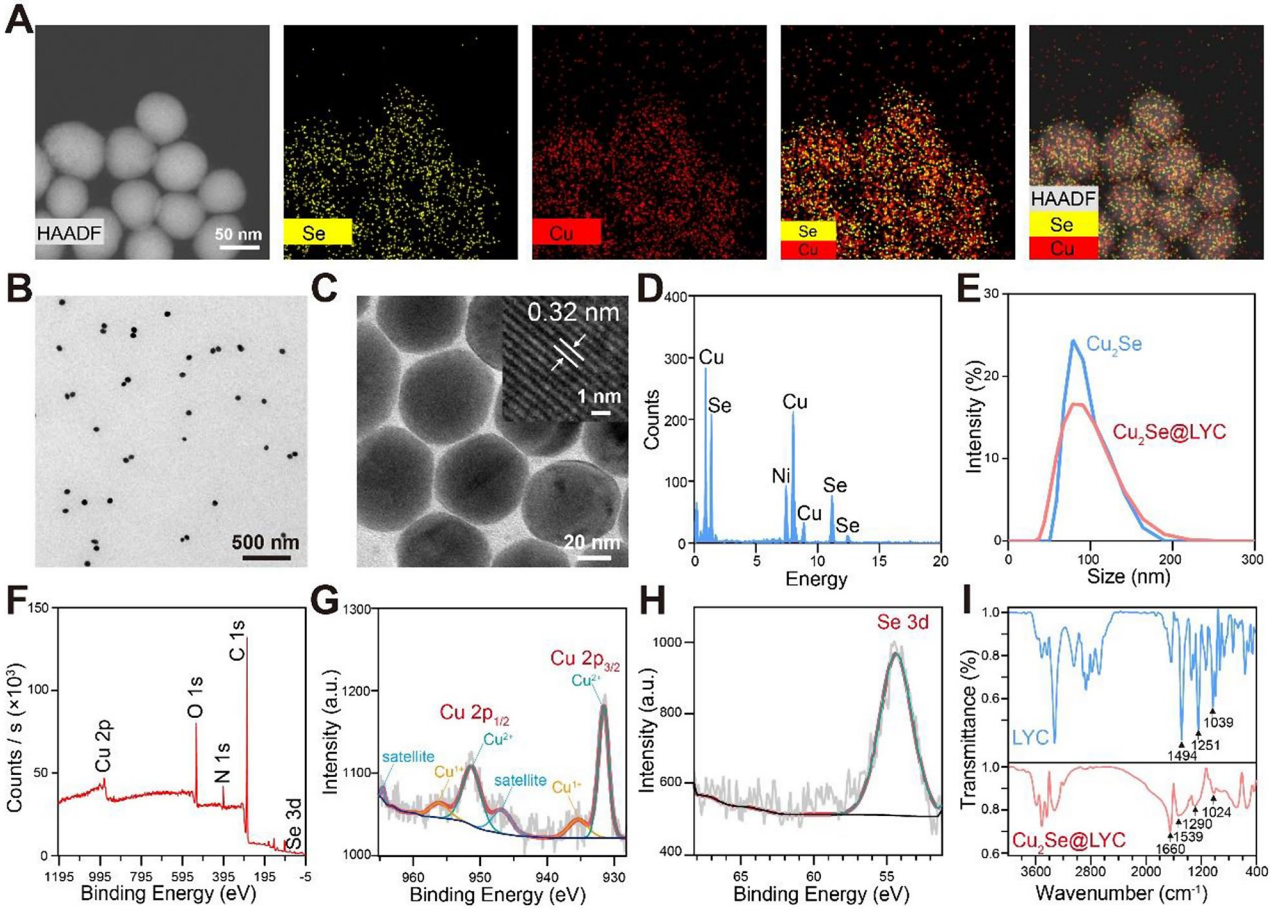

Fig. 1 Characterization of Cu2Se@LYC (**A**) High-angle annular dark-field TEM image and elemental mapping of Cu_2Se NPs. (**B**) TEM images of Cu_2Se NPs. (**C**) HRTEM image of Cu_2Se NPs with the detail and the interplanar spacing. (**D**) EDS mapping and (**E**) hydrodynamic diameter distribution of Cu_2Se NPs. XPS of (**F**) Cu_2Se, (**G**) Cu2p and (**H**) Se3d. (**I**) FTIR spectra of Cu_2Se and CL NPs

chemical state was further confirmed by satellite peaks observed at approximately 946.9 and 964.6 eV (Fig. 1G). In the Se 3d spectrum (Fig. 1H), a single broad peak is observed in the energy range of 52 to 58 eV, which corresponds well with the bimodal fitting of Se 3d5/2 (54.0 eV) and 3d3/2 peaks (54.5 eV), respectively. These characteristics suggest that the element with selenium proves a valence state of Se^{2-}. The Fourier transform infrared (FTIR) spectrum reveals the presence of three characteristic peak for LYC (Fig. 1I) [35]. The peak at 1251 cm^{-1} was attributed to the Ar-O stretching vibration (1270–1230 cm^{-1}) of the aromatic ether, while the peak at 1039 cm^{-1} corresponds to the R-O stretching vibration (1050–1000 cm^{-1}). The presence of a peak at 1494 cm^{-1} indicates the presence of an aromatic group C=C bond (1600–1450 cm^{-1}). The characteristic peaks of PVP are -C=O stretching vibration at -1660 cm^{-1} and -C-N-stretching vibration at 1290 cm^{-1}.[35] When LYC was conjugated with PVP, the composite NPs has a common crest of both, such as 1660 cm^{-1} and 1539 cm^{-1},1290 cm^{-1} and 1024 cm^{-1} (Fig. 1I).

The photothermal properties of Cu2Se@LYC

Cu_2Se was a typical photothermal conversion agent of NIR-II light and the CL was tailored for the therapy of HS, therefore the photothermal properties of CL was investigated. With the gradual increase in Cu_2Se concentration (10 to 160 μg/mL), the UV-vis-NIR spectra curve exhibits a pronounced upward shift within the NIR-II window (1000–1100 nm), accompanied by a prominent absorption peak (Additional fle: Fig. S4). As shown in Fig. 2A, the CL performs characteristic absorbed peaks

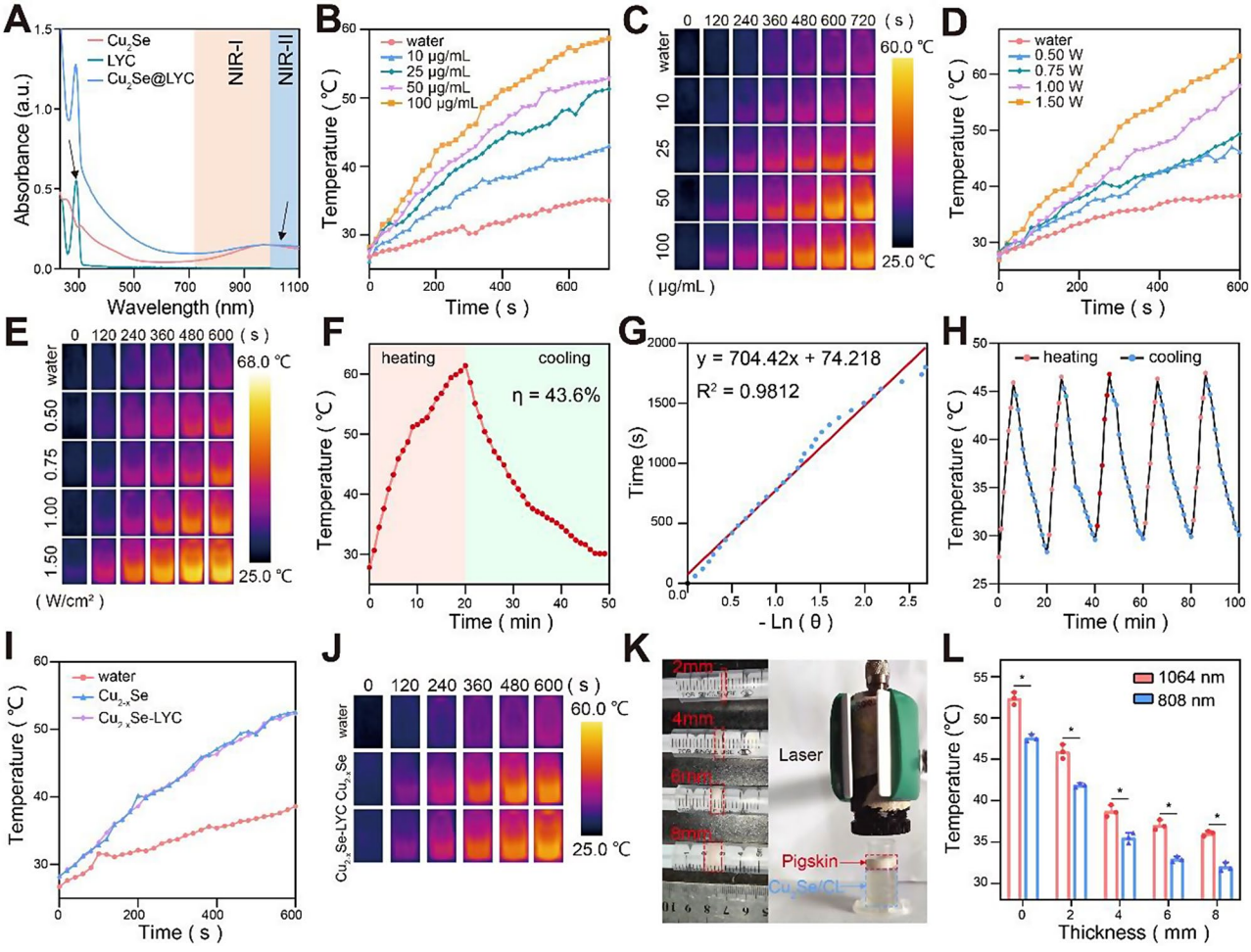

Fig. 2 Identification of photothermal properties of CL. (**A**) UV-vis-NIR spectra of Cu_2Se, lycorine and CL. (**B**) Temperature curves and (**C**) typical photothermal images of distilled water and different concentrations (10 μg/mL, 25 μg/mL, 50 μg/mL, and 100 μg/mL) of Cu_2Se under fixed 1064 nm laser irradiation (1.00 W/cm^2). (**D**) Temperature changes and (**E**) representative photothermal images of distilled water and 50 μg/mL Cu_2Se under different laser intensities (0.50, 0.75, 1.00, and 1.50 W/cm^2). (**F**,**G**) Photothermal conversion efficiency of Cu_2Se NPs. (**H**) Temperature change curve of photothermal stability of Cu_2Se. (**I**) The temperature rise curves and (**J**) photothermal images of distilled water, Cu_2Se, and CL under laser irradiation (1064 nm, 1.00 W/cm^2). (**K**) Schematic diagram of laser penetration detection. (**L**) The temperature changes of CL solution after two kinds (808 nm and 1064 nm) of laser penetrate pig skin of different thickness ($n = 3$). Data are presented as mean ± SD. # indicates $p < 0.05$

at 290 nm and 1000–1100 nm, which belonged to lycorine and Cu_2Se NPs, respectively. Various concentrations of Cu_2Se (dissolved in water) were subjected to a 1064 nm laser at 1.00 W/cm^2 for 12 min, and the resulting temperature changes were observed across different groups. After 12 min of irradiation, the temperature of all groups exhibited a time-dependent increase. Specifically, the solution temperature of 10 μg/mL, 25 μg/mL, 50 μg/mL, and 100 μg/mL of Cu_2Se rose from room temperature to 35.0℃, 43.0℃, 51.3℃,52.8℃ and 58.7℃ respectively (Fig. 2B, C), indicating that the temperature increases proportionally with the increase of Cu_2Se concentration, given the same irradiation time. Further, we applied varying irradiation powers (0.50, 0.75, 1.00, and 1.50 W/cm^2) to 50 μg/mL Cu_2Se solutions, these solutions were irradiated for a duration of 10 min and their respective temperature changes were monitored. The 1.50 W/cm^2 group exhibited the most pronounced temperature change compared to the water control group, reaching a peak temperature of 63.2℃ (Fig. 2D, E). Those data collectively indicate that Cu_2Se showed a favorable photothermal effect in the NIR-II region. Next, the Cu_2Se solution (50 μg/mL) was exposed to a 1.00 W/cm^2 laser for 20 min, resulting in an attained final temperature of 61.4℃ (Fig. 2F). Following a cooling period at ambient conditions for approximately 30 min, the temperature returned to room level. The photothermal conversion efficiency was calculated to be 43.6% (Fig. 2F, G). The photothermal stability was measured by subjecting Cu_2Se solution (50 μg/mL) to 5 consecutive cycles of NIR-II irradiation (heated for 5 min, cooled for 15 min), the result in Fig. 2H revealed its robust as a photosensitizer.

The photothermal properties of CL have also been examined, as depicted in Fig. 2I and J, the solution of CL also increased from 28.1℃ to 52.6℃ after laser radiation (1064 nm, 1.00 W/cm^2, 10 min), which was comparable with Cu_2Se NPs. The scars always appear on the skin surface and characterized by increased thickness and hardness compared to normal skin. The reported average thickness of HSs in humans from approximately 1.7 to 7.1 mm, with the thickest ones reaching close to 10 mm [36, 37]. Thus, the piercing depth of laser and temperature increase of scar location were highly related with the therapeutic efficiency. To investigate photothermal penetration capability of laser on HSs in vitro, as shown in Fig. 2K, the dermis of pig skin with varying thicknesses (2–8 mm) were obtained and placed on CL solution. The laser was then positioned on top of the pig skin, and the alteration in solution temperature was recorded. When utilizing a 1064 nm laser (1.00 W/cm^2, 10 min) for irradiating pig dermis with thicknesses of 2, 4, 6, and 8 mm, it was observed that the temperature of the CL solution increased about 45.9, 38.7, 36.9 and 36.0℃, respectively (Fig. 2L). Furthermore, considering the reported inhibitory effects of NIR-I lasers (808 nm) on HS [38], a comparative analysis was conducted to evaluate the transmission effects of the two lasers (808 nm and 1064 nm) on skin tissues. The photothermal effect induced by an 808 nm laser was found to be inferior compared to that of 1064 nm laser, with an average temperature decrease of 4℃ (Fig. 2L). The NIR-II laser, in summary, exhibits superior skin tissue penetration, thereby suggesting its potential for enhanced therapeutic efficacy on HS.

Biocompatibility of CL

The release capability of lycorine from CL NPs was assessed, revealing a 41.1%, 54.6% and 61.0% release rate after 2, 12 and 24 h, respectively (Additional fle: Fig. S6A and B). Next, we performed a comprehensive investigation on the uptake of CL NPs by fibroblasts, and upon Rhodamine B labeling of CL, fluorescence imaging demonstrated robust cellular uptake of CL (Additional fle: Fig. S5) following 2, 4, and 6 h of exposure. The electron microscopy analysis also revealed the intracellular presence of CL NPs within HSFs after 6 h of CL treatment (Fig. 3A). Then, the biocompatibility and cytotoxicity of NPs were tested. In order to better investigate the impact of NPs on HSFs, human dermal fibroblasts (HDFs, a normal dermal fibroblasts) and HaCaT (human keratinocyte) cell lines were employed as normal control groups. As depicted in Fig. 3B, CCK-8 assay results indicate that high concentrations of CL exhibit cytotoxicity towards HSFs, which may be related to the specific pro-apoptotic and anti-fibrotic abilities of lycorine. In contrast, HDFs and HaCaT cells showed excellent tolerance to both Cu_2Se and CL, as evidenced by cell viability exceeding 80% even at concentrations of up to 20 μg/mL (Additional fle: Fig. S7). High concentrations of CL (60 μg/mL) also have some cytotoxicity for HDFs and HaCaT cells, which may be related to LYC loading, which our previous study found can induce death of normal fibroblasts through apoptosis-related pathways [18]. The cell Live/Dead staining also indicated that Cu_2Se and CL had favorable biocompatibility with HDF and HaCaT cells (Additional fle: Fig. S8). This suggests that Cu2Se and CL have good biosafety towards normal skin cells.

CL activates apoptosis and ROS elevation of HSFs

Further, CCK8 assay was used to assess the cytotoxicity of Cu_2Se and CL at various concentrations (0, 2.5, 5, 10, 20, 40 and 60 μg/mL) without or with NIR-II (NIR-II+Cu2Se, NIR-II+CL) after treating HSFs for 24 h (Fig. 3C). Specifically, the cell viability of HSFs was 72.0% (NIR-II+Cu_2Se) and 68.7% (NIR-II+CL) at a concentration of 20 μg/mL. When the drug concentration was increased to 60 μg/mL, the cell viability of NIR-II+Cu_2Se and NIR-II+CL groups decreased to 54.0% and 36.6%,

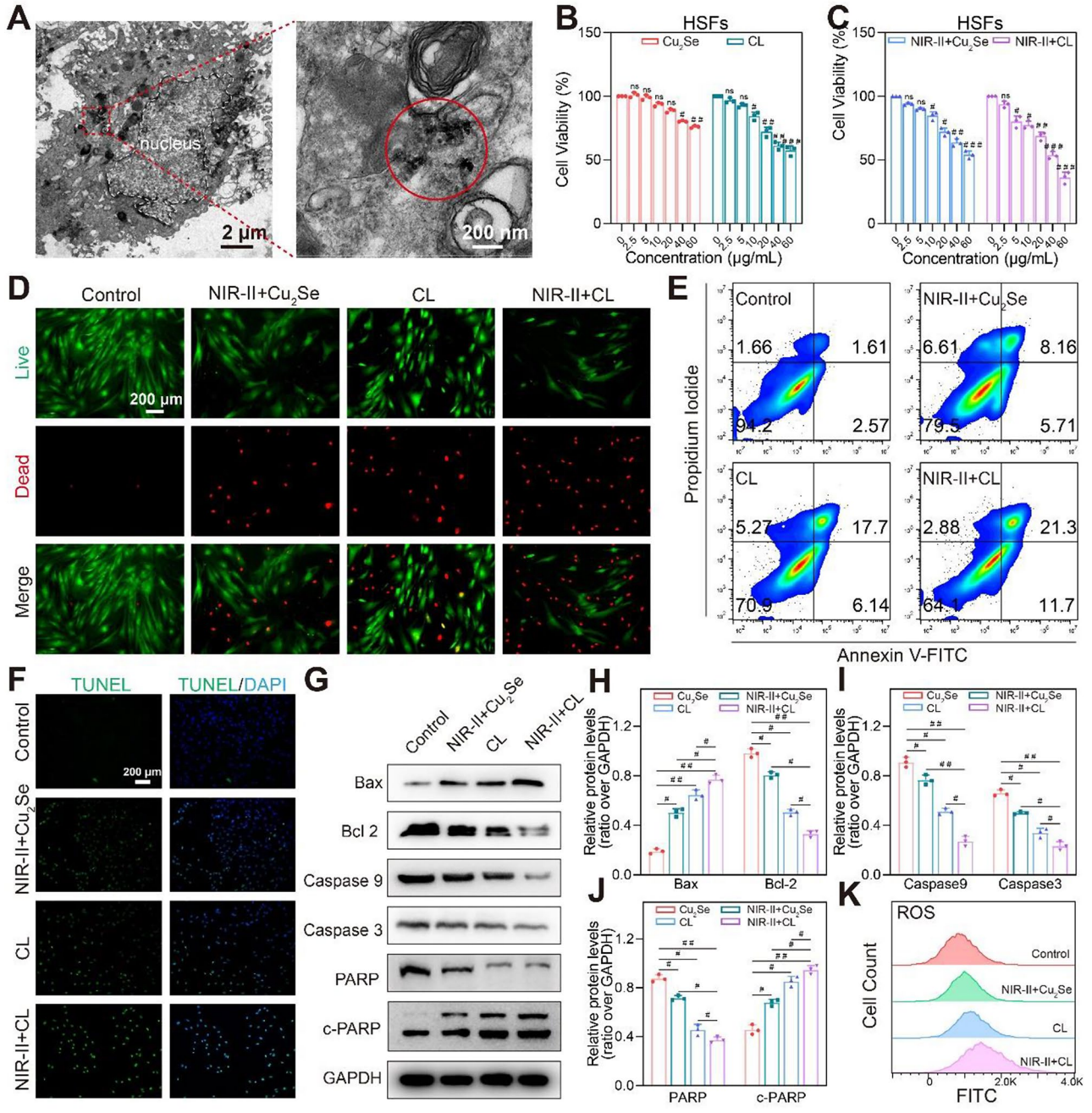

Fig. 3 The pro-apoptotic efficacy of CL NPs on HSFs in vitro. (**A**) Electron microscopy image depicting the uptake of CL NPs by HSFs. Cytotoxicity of Cu_2Se and CL combined with or without NIR-II to HSFs at different concentrations of for (**B**) 12 h and (**C**) 24 h ($n=3$). (**D**) Cell live/dead images under different treatments. (**E**) Flow cytometry images and (**F**) TUNEL staining images of apoptotic HSFs treated with Cu_2Se and CL with or without laser irradiation. (**G**) Western blot analysis of apoptosis-related proteins and (**H**-**J**) corresponding statistical results. (**K**) Flow cytometry analysis of ROS levels using the DCFH-DA probe under various treatments. Data are presented as mean ± SD. # indicates $p<0.05$; ## indicates $p<0.01$; ### indicates $p<0.001$. ns

respectively (Fig. 3C). The cell viability of the NIR-II group decreased by an average of 13.4% (Cu_2Se vs. NIR-II+Cu2Se) and 9.1% (CL vs. NIR-II+CL) under the same concentration. The fluorescence images of cell live and death under different treatment are shown in Fig. 3D, both the NIR-II+Cu_2Se group and LYC exhibited an increase in cell death, while the combined treatment of NIR-II and CL demonstrated the most pronounced induction of cellular demise. We next employed flow cytometry to assess the impact of different groups on the apoptotic rate, the control group exhibited a mere 4.18% apoptosis rate, whereas the NIR-II+Cu_2Se, CL and NIR-II+CL groups displayed significantly higher rates of 13.78%, 23.84%, and 34.0%, respectively (Fig. 3E,

Additional file: Fig. S9). Remarkably, NIR-II administration substantially augmented the apoptotic rate compared to CL alone. The pro-apoptotic ability of NIR-II was also demonstrated using TUNEL, revealing a gradual increase in the number of TUNEL-positive cells in the Control, NIR-II+Cu_2Se, CL, and NIR-II+CL groups (Fig. 3F). Further, the expression of apoptosis-related proteins in the 4 groups were detected. Compared to the control group, the NIR-II+Cu_2Se, CL, and NIR-II+CL groups exhibited increased expression of pro-apoptotic protein Bax, while the expression of anti-apoptotic protein Bcl-2 gradually decreased. Additionally, downstream caspase9 and caspase3 levels also showed a gradual decrease. Moreover, poly ADP-ribose polymerase (PARP), another apoptotic marker, underwent progressive degradation into c-PARP (Fig. 3G-J). In these groups, the NIR-II+CL group demonstrated the most significant alterations in those protein expression (Fig. 3G-J).

In our previous study, we have demonstrated that lycorine can enhance apoptosis by stimulating the generation of reactive oxygen species (ROS) [18]. Subsequently, the impact of different groups on reactive oxygen species (ROS) production in HSFs was assessed using flow cytometry. As shown in Fig. 3K, the ROS levels in the NIR-II+Cu_2Se, CL, and NIR-II+CL groups were were gradually increased compared with the control group. The data suggests that CL NPs has the potential to counteract the excessive proliferation of myofibroblasts by stimulating ROS production, thereby promoting apoptosis.

In addition to cell proliferation, the augmented migratory capacity of fibroblasts in HS is also a significant manifestation. Therefore, we conducted cell wound healing test and transwell assay to evaluate the migratory ability of fibroblasts. The cell mobility of the untreated group was 83.9%, whereas that of the NIR-II+Cu_2Se, CL and NIR-II+CL groups exhibited values of 64.6%, 51.8% and 35.0%, respectively (Additional file: Fig. S10A, B). The transwell assay exhibited a consistent pattern, the number of cells passing through the well in the control group was approximately 442 cells per field of view (FOV), which represented a 2.68-fold increase compared to that observed in the NIR-II+CL group (120 cells/FOV, Additional file: Fig. S11A, B).

CL promotes mitochondrial dysfunction and autophagic death in HSFs

To further validate the mechanism of CL in promoting apoptosis of HSFs, the mitochondrial membrane potential (MMP), cytochrome C expression and autophagy associated proteins were investigated. In Fig. 4A-C, the control group exhibits predominant red fluorescence, indicative of a normal MMP. Following 24 h of different treatments, JC-1 was observed to disperse as monomers throughout the cell, exhibiting green fluorescence indicative of a diminished mitochondrial membrane potential (Fig. 4A-C). The severity of mitochondrial damage is positively correlated with the Monomers/Aggregates ratio, and notably, the NIR-II+CL group exhibited the most pronounced variation in this ratio (Fig. 4B-D).

The release of cytochrome C from mitochondria into the cytoplasm is a key step in cell apoptosis. As depicted in Fig. 4E and F, both NIR-II and CL groups induced the translocation of cytochrome c when compared to the control group, with the most obvious effect observed in the NIR-II+CL group. Furthermore, electron microscopy analysis showed that the untreated HSFs exhibited healthy mitochondrial structure and morphology (green arrows), whereas the mitochondria in the NIR-II+CL and CL groups displayed swelling (red arrows) along with significant autophagosomes (yellow arrows) (Fig. 4G). Additionally, the cells in the NIR-II+CL group demonstrated numerous vacuoles (Fig. 4G).

The above results inspired us to further study the process of autophagy, which is a ubiquitous physiological mechanism for cellular self-degradation and metabolism, also plays a pivotal role in PCD. The autophagy associated proteins including beclin 1, LC3 and p62 were examined using western blot (Fig. 4H). Compared to the control group and the CL group, the expression of beclin 1 and the LC3-II/LC3-I ratio were upregulated in the NIR-II+Cu_2Se group and the NIRL-II+CL group, respectively, while the expression of p62 was decreased, indicating that NIR-II enhanced autophagy levels in HSFs (Additional file: Fig. 4H, S12). Immunofluorescence staining of LC3-II also indicated a significant increase in autophagosomes (green puncta, Fig. 4I). Recent studies have shown that lycorine can promote autophagy and apoptosis of human hepatocellular carcinoma cells through the Akt/mTOR pathway [39]. We further investigated the impact of CL on autophagy in HSFs and observed an increase in LC3-II/LC3-I ratio and a decrease in p62 protein level with increasing concentrations (Additional file: Fig. S13A-D). Additionally, immunofluorescence analysis revealed an elevation of LC3-II puncta within cells as the concentration gradient of lycorine increased (Additional file: Fig. S13E). Collectively, the above data made it certain that the combination of NIR-II and CL induces death of HSFs by augmenting autophagy, which was illustrated in Fig. 4J.

CL weakens the fibrotic level of HSFs

Apart from immoderate proliferation of myofibroblasts, the contractile properties and the excessive deposition of collagen in their extracellular matrix are also prominent features of fibrosis. Fibrosis markers such as α-SMA is highly expressed in myofibroblasts, which enhances the contractility of the cells and is clinically manifested as

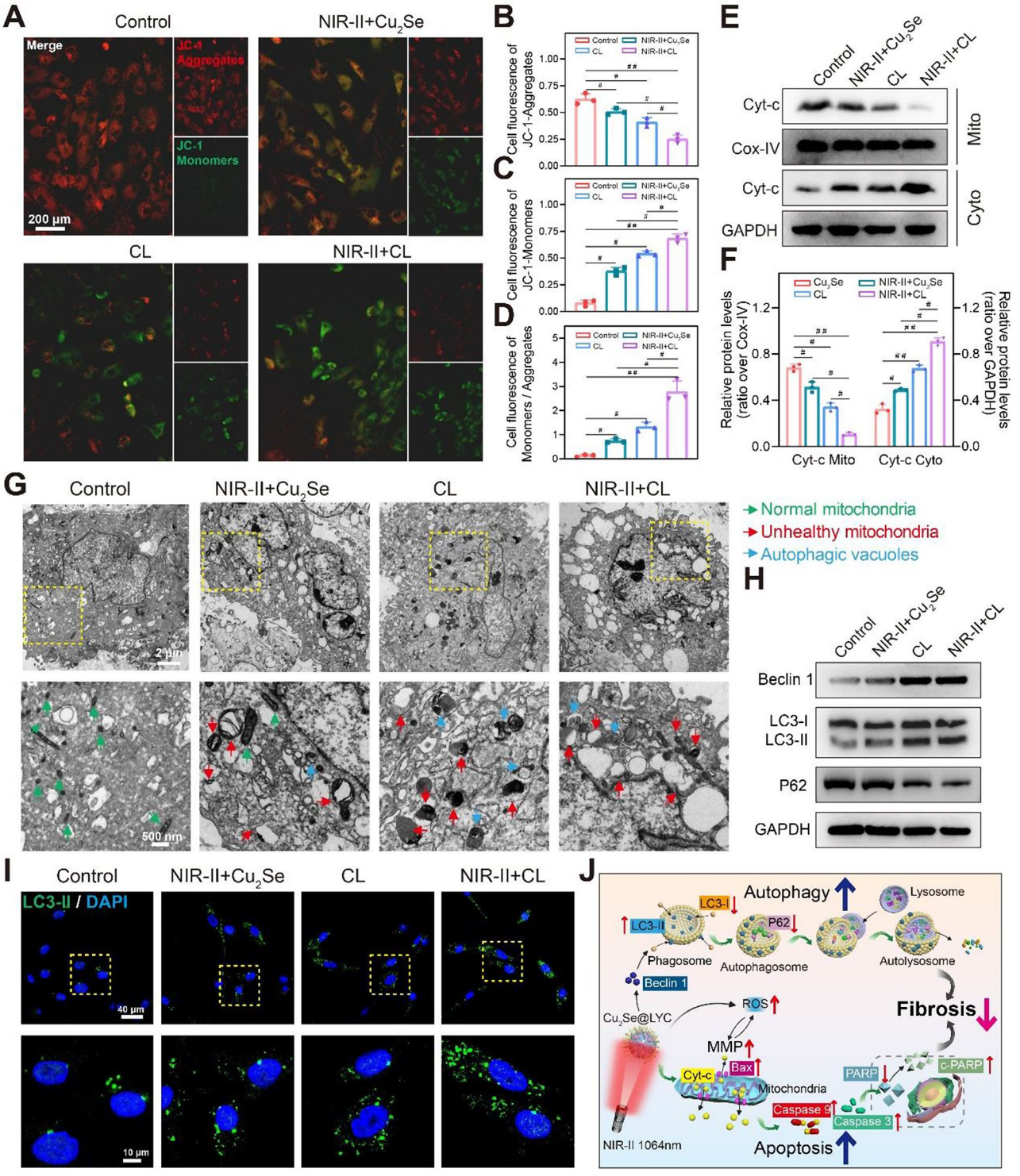

Fig. 4 The combination of NIR-II and CL induced mitochondrial damage and triggered autophagy-mediated cell death. (**A**) Representative fluorescent image of cells labeled with JC-1 under different treatments and (**B**-**D**) their statistical results. (**E**) Western blot analysis and (**F**) Statistical analysis of cytochrome-c protein expression in cytoplasm and mitochondria of HSFs exposed to laser irradiation or NPs treatments. (**G**) Bio-TEM images of mitochondria and autophagosome microstructure of cells in different treatment groups (green arrow: healthy mitochondria; red arrow: unhealthy mitochondria; yellow arrow: autophagic vacuoles). (**H**) Western blot results of autophagy associated proteins (Beclin 1, LC3 and P62). (**I**) Immunofluorescence staining image of LC3-II after Cu_2Se and CL treatemnts with or without laser irradiation. (**J**) The mechanism diagram of IR-II combined with CL promoting autophagic death. Data are presented as mean ± SD. # indicates $p < 0.05$; ## indicates $p < 0.01$; ### indicates $p < 0.001$

scar contracture deformity [16, 40]. As shown in Fig. 5A, we mixed fibroblasts with mouse tail collagen and subsequently cultured in a suitable medium. After 24-hour treatment, cellular contraction led to a significant reduction in the area of the collagen gel. The collagen contraction assay revealed that the control group exhibited a contraction rate of 73.43%, whereas the NIR-II+Cu_2Se, CL, and NIR-II+CL groups demonstrated contraction rates of 49.17%, 32.47%, and 22.30% respectively, indicating a significant attenuation in the contraction ability of HSFs upon exposure to NIR-II and CL (Fig. 5B, C). Subsequently, immunofluorescence and western blot analysis were employed to detect the fibrotic markers Collagen I and III, which are key components of the ECM, as well as α-SMA, a crucial marker for myofibroblasts. Both immunofluorescence (Fig. 5D) and western blot (Fig. 5E-H) results demonstrated that treatments with NIR-II+Cu_2Se, CL, and NIR-II+CL attenuated the expression of Collagen I, Collagen III, and α-SMA in HSFs to varying extents. In comparison to the exclusive utilization of NIR-II+Cu_2Se, the incorporation of LYC significantly enhances its anti-fibrotic efficacy.

CL inhibits the scarring formation in vivo

After the inhibitory effect of NIR-II combined with CL towards HSFs have been confirmed, subsequently, we established a rabbit ear model of hypertrophic scars in vivo. The ventral side of rabbit ears was subjected to four 10 mm diameter wounds, wherein the epidermis and dermis of the skin were meticulously excised, which is one of the most classic animal models of scarring, as depicted in Fig. 6A [41, 42]. After 14 days following the operation, the wound exhibited significant healing and started to develop hypertrophic scars. These scars were

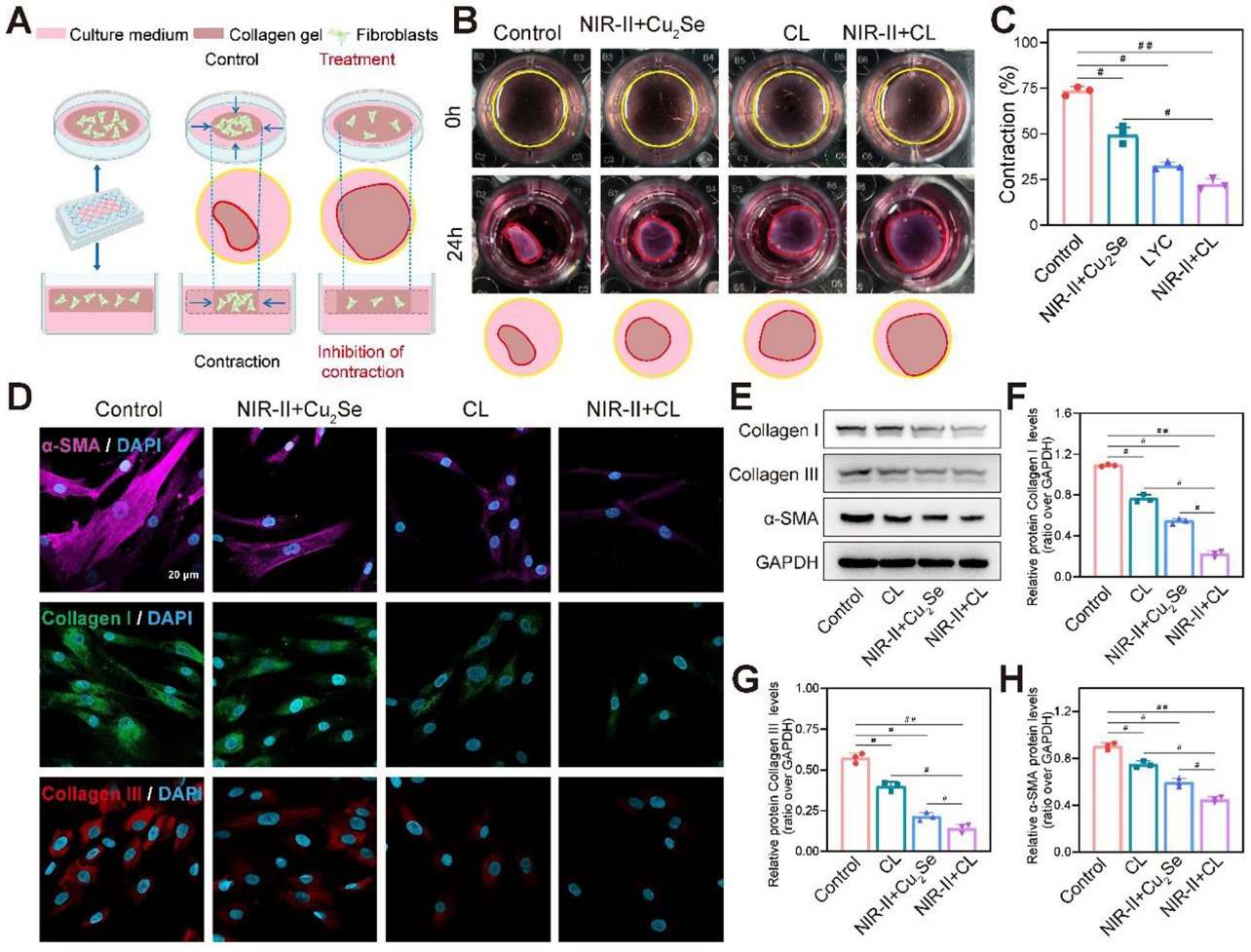

Fig. 5 1064 nm laser-assisted lycorine therapy effectively mitigates fibrotic levels in HSFs. (**A**) Schematic illustration of collagen gel contraction assay. (**B**) The image of HSFs cultured in rat tail collagen after different treatments. (**C**) Statistical analysis of the collagen contraction rate. (**D**) Immunofluorescence staining images of typical fibrosis markers (α-SMA, Collagen I, Collagen III) in HSFs exposed to or without laser light combine with Cu_2Se and CL. (**E**) western blot assay data and (**F**-**H**) statistical calculation on the expression levels of α-SMA, Collagen I, and Collagen III in HSFs after treatment with different formulations. Data are presented as mean ± SD. ns indicates no significance, # indicates $p < 0.05$; ## indicates $p < 0.01$; ### indicates $p < 0.001$

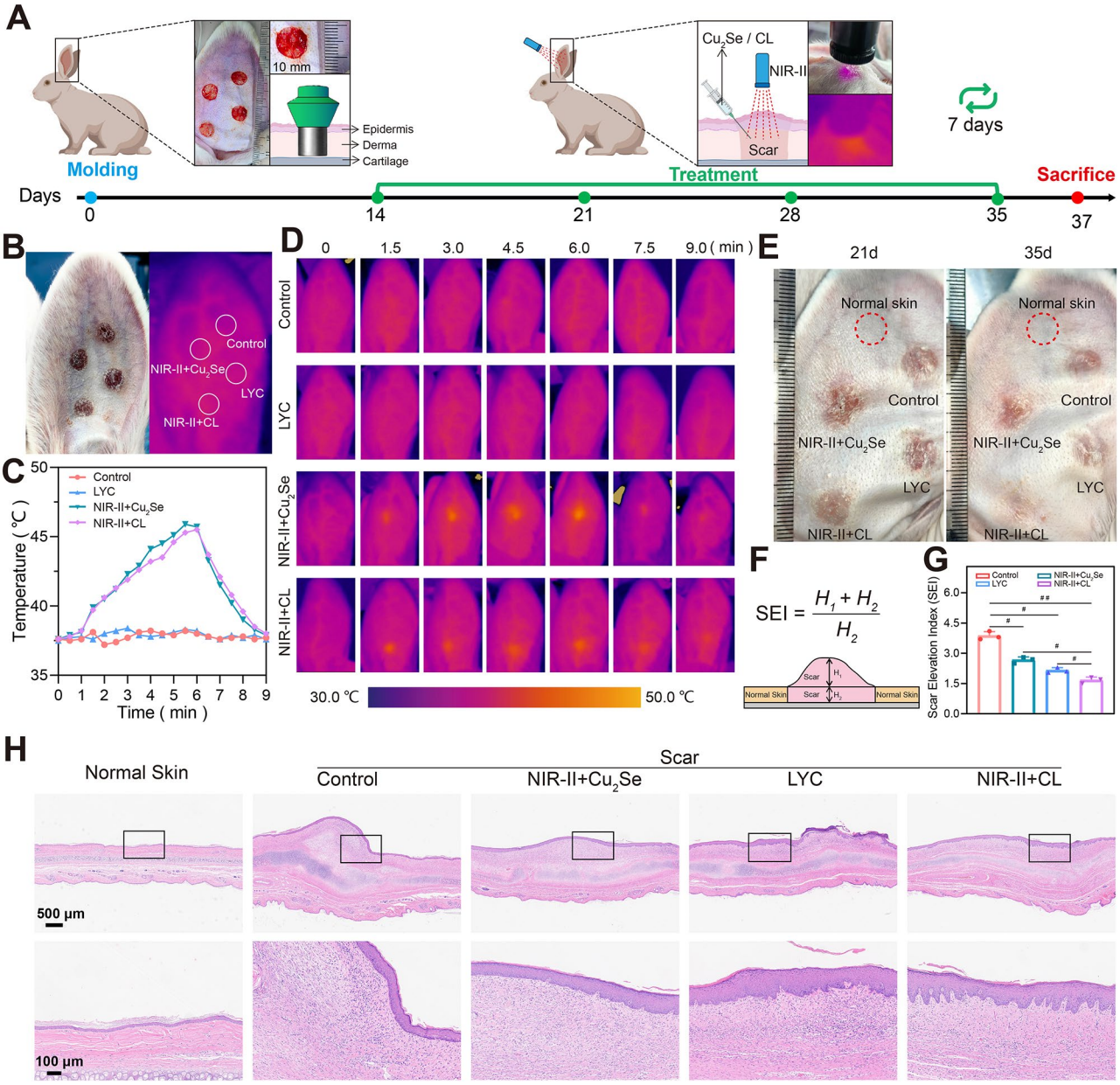

Fig. 6 Photothermal properties of CL and its effect on rabbit ear scars in vivo (**A**) Timeline and schematic diagram of rabbit ear scar modeling and treatment. (**B**) Image of grouping distribution on rabbit ear scars 14 days after modeling. (**C**) The temperature change curve and (**D**) photothermal image in various treatment groups were acquired within 9 min (heating 6 min, cooling 3 min), with or without laser irradiation laser irradiation. (**E**) A follow-up image of the appearance of scar in rabbit ears after 1 - and 3-week treatment. (**F**) Diagram of scar elevation index calculation (SEI). (**G**) SEI assay calculated from HE staining. (**H**) H&E staining images of rabbit ear scars after different treatments. Data are presented as mean ± SD. # indicates $p < 0.05$; ## indicates $p < 0.01$; ### indicates $p < 0.001$

visibly prominent on the skin surface, displaying a purplish-red coloration and a hardened texture, indicating the successful modeling (Fig. 6B). Starting from day 14, the four wounds of each ear were divided into four groups and subjected to different treatments as follows: (1) control group: 0.1 mL of normal saline was injected into scar only; (2) NIR-II+Cu_2Se group: ear scar underwent subcutaneous injection of Cu_2Se (0.1 mL,10 mg/mL) along with 5 min of weekly NIR-II laser irradiation (0.5 W/cm^2,1064 nm); (3) CL group: scar region was injected with 0.1 mL of CL (10 mg/mL); (4) NIR-II+CL group: CL (0.1 mL,10 mg/mL) was injected and the same laser irradiation as the CL group was operated every week (Fig. 6B). The follow-up period extended until day 35 after the surgery (Fig. 6A). Firstly, the temperature change of scars under the injection of CL and irradiation of NIR-II was measured. Figure 6C demonstrated that the temperature of NIR-II groups (NIR-II+Cu_2Se group

and NIR-II+CL group) gradually increased, while the other two groups hardly changed. The photothermal map of rabbit ear demonstrated that after 6 min of irradiation, the highest temperature reached 45℃, providing strong effect of photothermal (Fig. 6C, D). About 3 min after stopping the laser irradiation, the temperature of rabbit ears returned to normal body temperature (Fig. 6C, D). The findings suggest that NIR-II irradiation combined with CL treatment demonstrates effective laser transmission in vivo and has the potential to induce apoptosis and autophagy-mediated death of fibroblasts within rabbit ear scar.

Follow-up photos were taken to assess the appearance of rabbit ears as treatment progressed. On the 21st day post-surgery, scar bulging was evident and exhibited a more intense red color in the control group. In contrast, smoother scarring was observed in the NIR-II+Cu_2Se, CL, and NIR-II+CL groups (Fig. 6E). By day 35th, scars in the NIR-II+CL group appeared lighter and predominantly flat (Fig. 6E). The scar elevation index (SEI), as a commonly used scar evaluation indicator, is directly proportional to the thickness of the scar (Fig. 6F). The greater the SEI value, the more prominent the hypertrophic scar. According to the results of H&E pathological staining, the SEI values were calculated for the control group (3.87), NIL-II+Cu_2Se group (2.67), CL group (2.15), and NIL-II+CL group (1.67) (Fig. 6G). The H&E staining revealed disorganized and abundant accumulation of dermal collagen fibers in the control group, whereas the experimental group exhibited neatly arranged collagen fibers (Fig. 6H).

Furthermore, the biocompatibility of CL was tested. The hemolysis assay revealed that concentrations of CL ranging from 0 to 40 μg/mL did not induce cellular hemolysis (Additional file: Fig. S14). The H&E staining of the heart, liver, spleen, lung, and kidney from different treated rabbits revealed no significant differences between the control group and each experimental group and there was no evidence of organ injury, infection, or inflammation (Additional file: Fig. S15).

CL reduces fibrotic level of rabbit ear scars in vivo

Next, the scar tissue of rabbit ear was sampled 35 days post-surgery, followed by the assessment of fibrosis, apoptosis, and autophagy-related parameters. The results of Masson's trichrome staining revealed that the proportion of collagen (blue for collagen fiber, red for nucleus) in the NIR-II+CL group was significantly lower compared to the other three groups (Additional file: Fig. S16A, B). The picrosirius red dye, known for its ability of binding with collagen molecules and resulting in a distinct bright red appearance of collagen under an ordinary light microscope, was used for collagen detection. The proportions of picrosirius red in the control, NIR-II+Cu_2Se, CL, and NIR-II+CL groups were 86.3%, 72.7%, 63.3%, and 54.0% respectively (Additional file: Fig. S17A, B). When observing the picrosirius red staining under a polarized light microscope, type I collagen fibers exhibited shades of orange-yellow or red and type III collagen fibers appeared green in color. In the control group, in Fig. 7A and B, type I collagen exhibited dominance while type III collagen played a supplementary role, with nearly 80% of positive picrosirius red staining observed. However, following the injection of Cu_2Se into the rabbit ear scar and subsequent irradiation with NIR-II, there was an 18.7% reduction in the proportion of positive picrosirius red staining (Fig. 7A and B). Injection of CL alone also significantly decreased collagen content compared to the untreated group, whereas the NIR-II+CL group demonstrated the lowest collagen content (37.5%). In order to observe the decrease of collagen in a more detailed manner, immunohistochemical staining was performed on scar tissue, revealing a reduction in the expression of type I and type III collagens across all treatment groups (Additional file: Fig. S18A-D). Notably, the NIR-II+CL group exhibited the most pronounced decrease in collagen expression. Immunofluorescence staining of type I collagen corroborated these findings (Fig. 7C, D). Furthermore, we also investigated matrix metalloproteinase 3 (MMP3), an enzyme capable of degrading collagen in the ECM. Immunohistochemical findings indicated that both NIR-II and CL or their combined treatment resulted in increased MMP3 expression, subsequently leading to collagen degradation (Additional file: Fig. S18E, F).

In addition to collagen, α-SMA serves as a crucial indicator of hypertrophic scar fibrosis. Immunofluorescence analysis revealed that the fluorescence intensity in each experimental group was comparatively lower than that observed in the control group (Fig. 7E, F). Similarly, immunohistochemical results demonstrated a consistent trend (Additional file: Fig. S18G, H). Transforming growth factor-β1 (TGF-β1), as a cytokine that can promote fibroblast proliferation and phenotypic transformation, is able to transform normal fibroblasts into myofibroblasts and induce collagen production. The expression of TGF-β1 was significantly downregulated in the three treatment groups compared to the control group (Fig. 7G, H). Overall, the NIR-II demonstrated a favorable anti-skin fibrosis effect, with the inclusion of lycorine further augmenting the therapeutic effect of NIR-II.

The impact of this treatment system in vivo on pro-apoptotic and autophagic cell death was also assessed. The TUNEL staining was performed on sections of rabbit ear scar tissue treated with NIR-II or combined CL. It was observed that the TUNEL positive rate of cells in the control group was less than 1%, whereas it approached 2% in the NIR-II+Cu_2Se group, and reached as high as 5.8% and 8.5% in the CL group and NIR-II+CL group,

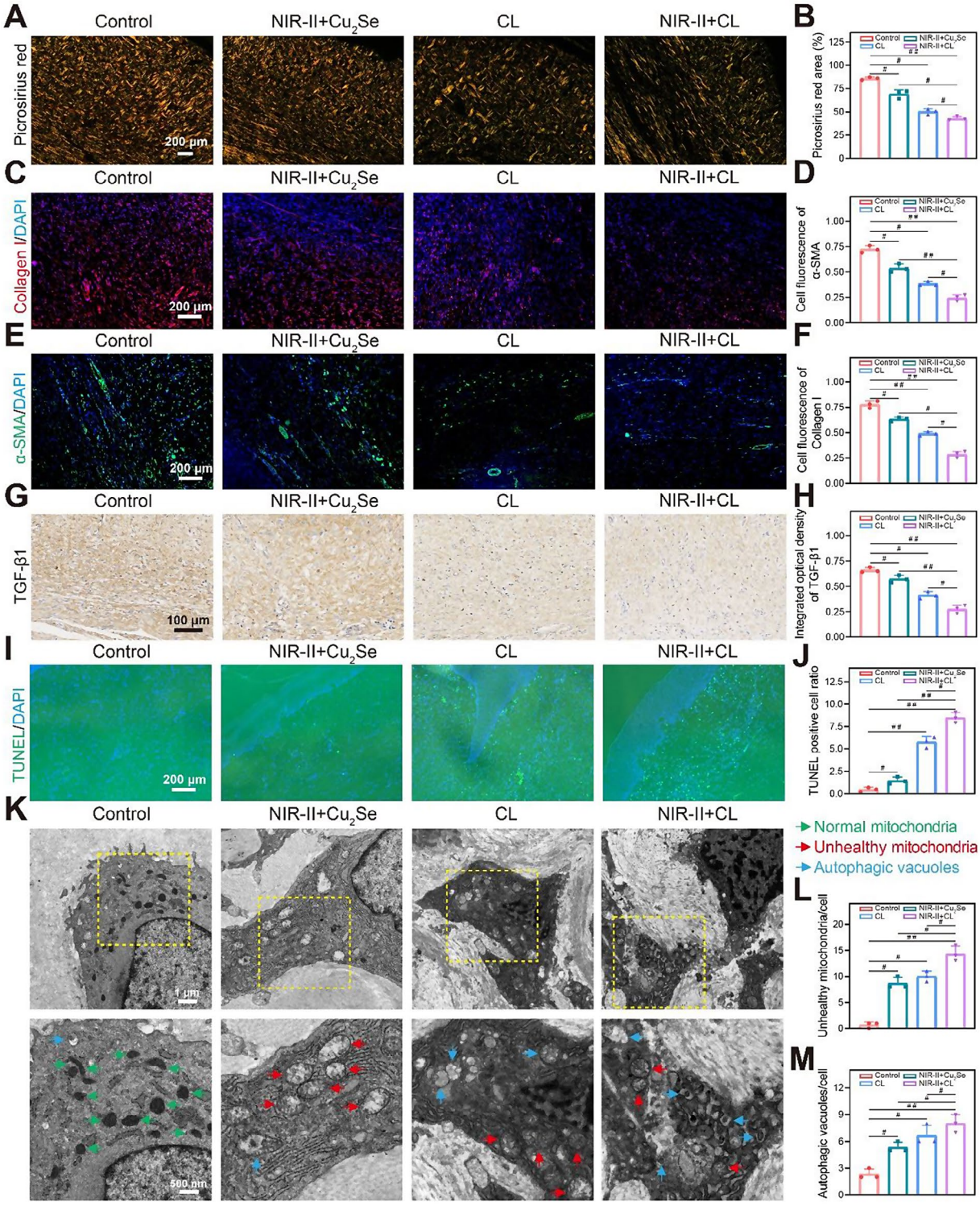

Fig. 7 Impact of a photothermal therapy system on fibroblast fibrosis and autophagic cell death in rabbit ear scars in vivo. (**A**) Representative picrosirius red stained images under polarized light of rabbit ear scars in different treatment groups ($n = 3$) and (**B**) its statistical analysis results. Immunofluorescence staining images and statistical analysis of fluorescence intensity of Collagen I (**C**, **D**) and α-SMA (E, F) in rabbit ear scar tissues ($n = 3$). (**G**) Immunohistochemical staining images of TGF-β1 in different treatment groups of rabbit ear scars ($n = 3$). (**H**) Results of statistical analysis of TGF levels. (**I**, **J**) Representative images of TUNEL staining and statistically analysis of rabbit ear scars after Cu_2Se, CL treatment and with or without laser irradiation ($n = 3$). (**K**) Electron microscope images showed the microstructure of rabbit ear scar tissue after different treatments (green arrow: healthy mitochondria; red arrow: unhealthy mitochondria; yellow arrow: autophagic vacuoles, $n = 3$). (**L**, **M**) Calculation of the number of unhealthy mitochondria and autophagy vacuoles. Data are presented as mean ± SD. ns indicates no significance, # indicates $p < 0.05$; ## indicates $p < 0.01$; ### indicates $p < 0.001$

respectively (Fig. 7I, J). Finally, electron microscopy was employed to examine the cellular microstructure in rabbit ear tissue, as depicted in Fig. 7K. The mitochondria of the control group exhibited a predominantly normal and healthy morphology (green cusps), with a limited presence of physiological autophagy vesicles (yellow cusps). The NIR-II+Cu_2Se group exhibited a higher proportion of unhealthy mitochondria (indicated by red cusps), and the mitochondrial ridge displayed reduced prominence and structural swelling (Fig. 7K, L). In addition to inducing mitochondrial damage, the CL group and NIR-II+CL group exhibited a gradual increase in the number of autophagosomes, indicating that lycorine and photothermal effect synergistically promoted the augmentation of autophagy flux (Fig. 7L, M). The nuclei of both the CL group and the NIR-II+CL group exhibited significant wrinkling, along with the formation of vacuoles, indicative of cellular death (Fig. 7K). The aforementioned evidence elucidates that the combined action of NIR-II and CL leads to a reduction in the population of fibroblasts through synergistic promotion of autophagic cell death, consequently diminishing their proliferative capacity.

Conclusion

In summary, the CL NPs, characterized by a particle size of 90.25 nm and a Zeta potential of -30.7 mV, were synthesized using Cu_2Se NPs and LYC, exhibiting satisfactory anti-fibrosis functionality with the assistance of IR-II light. First, CL possesses excellent photothermal properties and laser transmission capability to effectively pierce 10 mm of dermis. Mechanistically, when combined with NIR-II irradiation, CL induces ROS generation, disrupts mitochondrial function, triggers cytochrome C translocation to the cytoplasm, initiates a cascade reaction involving downstream Caspases, and ultimately leads to endogenous apoptosis. Simultaneously, CL also demonstrates remarkable potential in activating autophagic cell death. In terms of anti-fibrotic effects, CL significantly attenuates collagen contractility in HSFs while reducing the expression levels of collagen I/III and α-SMA. Finally, in the rabbit ear scar model, CL facilitates fibroblast autophagy and attenuates the expression of fibrotic markers, demonstrating commendable anti-scarring efficacy in vivo. Since the maximum thickness of the rabbit ear scar model is about 3 mm, the scar with sufficient thickness has not been adequately verified in vivo, necessitating more experiments in the future. Compared to existing laser therapy, this treatment offers enhanced skin penetration, especially for HS. It is expected that CL+NIR-II is a novel therapeutic approach for HS with substantial clinical translational implications.

Supplementary Information

The online version contains supplementary material available at https://doi.org/10.1186/s12951-024-02876-9.

Supplementary Material 1

Acknowledgements
This work was supported by the Postdoctoral Workstation Project of Guangdong Second Provincial General Hospital (Grant number: 2023BSGZ013).

Author contributions
Y. D., H.W. and Y. Z. contributed equally to this work. Y. D. and H.W. were responsible for data acquisition, analysis and drafting the article; Y. D., Y. Z., Y.W., Z.L., H.Y., S.O. and Z.S. performed the experiments. L.L., J.T., Z.H., D.L., Y.R. and Z.Z. provided advice for the design of the study. P.Z., B.T. and S.L. were responsible for the conception, design and supervision of the study.

Funding
This work was supported by the Postdoctoral Workstation Project of Guangdong Second Provincial General Hospital (Grant number: 2023BSGZ013).

Data availability
No datasets were generated or analysed during the current study.

Declarations

Ethics approval and consent to participate
This study was approved by the Ethics Committee for Clinical Research and Animal Trials of Guangdong Second Provincial General Hospital (Guangzhou, China, approval number: 2023-DW-KZ-034), and written informed consent was obtained from all participants.

Consent for publication
All authors have read and approved the manuscript.

Competing interests
The authors declare no competing interests.

Received: 2 June 2024 / Accepted: 26 September 2024
Published online: 15 October 2024

References

1. Finnerty CC, Jeschke MG, Branski LK, Barret JP, Dziewulski P, Herndon DN. Hypertrophic scarring: the greatest unmet challenge after burn injury. Lancet. 2016;388(10052):1427–36.
2. Ogawa R. The most current algorithms for the Treatment and Prevention of Hypertrophic Scars and keloids: a 2020 update of the algorithms published 10 years ago. Plast Reconstr Surg. 2022;149(1):e79–94.
3. Obaidi N, Keenan C, Chan RK. Burn Scar Management and reconstructive surgery. Surg Clin North Am. 2023;103(3):515–27.
4. Fernandez-Guarino M, Bacci S, Perez Gonzalez LA, Bermejo-Martinez M, Cecilia-Matilla A, Hernandez-Bule ML. The role of physical therapies in Wound Healing and assisted scarring. Int J Mol Sci 2023;24(8).
5. Shi N, Wang Y, Xia Z, et al. The regulatory role of the apelin/APJ axis in scarring: identification of upstream and downstream mechanisms. Biochim Biophys Acta Mol Basis Dis. 2024;1870(4):167125.
6. Altemir A, Boixeda P. Laser treatment of burn scars. Actas Dermosifiliogr. 2022;113(10):938–44.
7. Leszczynski R, da Silva CA, Pinto A, Kuczynski U, da Silva EM. Laser therapy for treating hypertrophic and keloid scars. Cochrane Database Syst Rev. 2022;9(9):CD011642.
8. Karmisholt KE, Haerskjold A, Karlsmark T, Waibel J, Paasch U, Haedersdal M. Early laser intervention to reduce scar formation - a systematic review. J Eur Acad Dermatol Venereol. 2018;32(7):1099–110.

9. Nobari NN, Tabavar A, Sadeghi S, et al. A systematic review of the comparison between needling (RF-needling, meso-needling, and micro-needling) and ablative fractional lasers (CO(2), erbium YAG) in the treatment of atrophic and hypertrophic scars. Lasers Med Sci. 2023;38(1):67.
10. Zhang DD, Zhao WY, Fang QQ, et al. The efficacy of fractional CO(2) laser in acne scar treatment: a meta-analysis. Dermatol Ther. 2021;34(1):e14539.
11. Yin J, Zhang S, Yang C, et al. Mechanotransduction in skin wound healing and scar formation: potential therapeutic targets for controlling hypertrophic scarring. Front Immunol. 2022;13:1028410.
12. Wang ZC, Zhao WY, Cao Y, et al. The roles of inflammation in Keloid and hypertrophic scars. Front Immunol. 2020;11:603187.
13. Joorabloo A, Liu T. Recent advances in nanomedicines for regulation of macrophages in wound healing. J Nanobiotechnol. 2022;20(1):407.
14. Yuan B, Upton Z, Leavesley D, Fan C, Wang XQ. Vascular and collagen target: a rational Approach to Hypertrophic Scar Management. Adv Wound Care (New Rochelle). 2023;12(1):38–55.
15. Hong YK, Chang YH, Lin YC, Chen B, Guevara BEK, Hsu CK. Inflammation in Wound Healing and pathological scarring. Adv Wound Care (New Rochelle). 2023;12(5):288–300.
16. Limandjaja GC, Belien JM, Scheper RJ, Niessen FB, Gibbs S. Hypertrophic and keloid scars fail to progress from the CD34(-) /alpha-smooth muscle actin (alpha-SMA)(+) immature scar phenotype and show gradient differences in alpha-SMA and p16 expression. Br J Dermatol. 2020;182(4):974–86.
17. Han F, Wang K, Shen K, et al. Extracellular vesicles from Lactobacillus druckerii inhibit hypertrophic scar fibrosis. J Nanobiotechnol. 2023;21(1):113.
18. Dong Y, Lv D, Zhao Z, Xu Z, Hu Z, Tang B. Lycorine inhibits hypertrophic scar formation by inducing ROS-Mediated apoptosis. Front Bioeng Biotechnol. 2022;10:892015.
19. Wu T, Hou X, Li J, et al. Microneedle-mediated Biomimetic Cyclodextrin Metal Organic frameworks for active targeting and treatment of hypertrophic scars. ACS Nano. 2021;15(12):20087–104.
20. Dong Y, Cao X, Huang J, et al. Melatonin inhibits fibroblast cell functions and hypertrophic scar formation by enhancing autophagy through the MT2 receptor-inhibited PI3K/Akt /mTOR signaling. Biochim Biophys Acta Mol Basis Dis. 2024;1870(1):166887.
21. Kim KH, Lee MS. Autophagy–a key player in cellular and body metabolism. Nat Rev Endocrinol. 2014;10(6):322–37.
22. Levine B, Kroemer G. Biological functions of Autophagy genes: a Disease Perspective. Cell. 2019;176(1–2):11–42.
23. Deng W, Shang H, Tong Y, et al. The application of nanoparticles-based ferroptosis, pyroptosis and autophagy in cancer immunotherapy. J Nanobiotechnol. 2024;22(1):97.
24. Liu S, Yao S, Yang H, Liu S, Wang Y, Autophagy. Regulator of cell death. Cell Death Dis. 2023;14(10):648.
25. Gordy C, He YW. The crosstalk between autophagy and apoptosis: where does this lead? Protein Cell. 2012;3(1):17–27.
26. Denton D, Kumar S. Autophagy-dependent cell death. Cell Death Differ. 2019;26(4):605–16.
27. Gundamaraju R, Lu W, Paul MK, et al. Autophagy and EMT in cancer and metastasis: who controls whom? Biochim Biophys Acta Mol Basis Dis. 2022;1868(9):166431.
28. Quarato G, Mari L, Barrows NJ, et al. Mitophagy restricts BAX/BAK-independent, parkin-mediated apoptosis. Sci Adv. 2023;9(21):eadg8156.
29. Zhang Q, Wang M, Deng X, et al. Shikonin promotes hypertrophic scar repair by autophagy of hypertrophic scar-derived fibroblasts. Acta Cir Bras. 2023;38:e384623.
30. Chen H, Xu K, Sun C, Gui S, Wu J, Wang S. Inhibition of ANGPT2 activates autophagy during hypertrophic scar formation via PI3K/AKT/mTOR pathway. Bras Dermatol. 2023;98(1):26–35.
31. Liu T, Ma X, Ouyang T, et al. Efficacy of 5-aminolevulinic acid-based photodynamic therapy against keloid compromised by downregulation of SIRT1-SIRT3-SOD2-mROS dependent autophagy pathway. Redox Biol. 2019;20:195–203.
32. Song Z, Zhao L, Liu J, et al. Glioma cell membrane camouflaged Cinobufotalin Delivery System for Combinatorial Orthotopic Glioblastoma Therapy. Nano Res. 2023;16(8):11164–75.
33. Xu H, Deng H, Ma X, et al. NIR-II-absorbing diimmonium polymer agent achieves excellent photothermal therapy with induction of tumor immunogenic cell death. J Nanobiotechnol. 2023;21(1):132.
34. Hu H, Yang W, Liang Z, et al. Amplification of oxidative stress with lycorine and gold-based nanocomposites for synergistic cascade cancer therapy. J Nanobiotechnol. 2021;19(1):221.
35. Chen Z, Ye X, Yuan K, et al. Lycorine nanoparticles induce apoptosis through mitochondrial intrinsic pathway and inhibit Migration and Invasion in HepG2 cells. IEEE Trans Nanobiosci. 2022;21(4):549–59.
36. Wiseman J, Ware RS, Simons M, et al. Effectiveness of topical silicone gel and pressure garment therapy for burn scar prevention and management in children: a randomized controlled trial. Clin Rehabil. 2020;34(1):120–31.
37. Kemp Bohan PM, Cooper LE, Lu KN, et al. Fractionated ablative Carbon Dioxide Laser Therapy decreases Ultrasound Thickness of Hypertrophic burn scar: a prospective process improvement Initiative. Ann Plast Surg. 2021;86(3):273–8.
38. Yu Z, Meng X, Zhang S, et al. IR-808 loaded nanoethosomes for aggregation-enhanced synergistic transdermal photodynamic/photothermal treatment of hypertrophic scars. Biomater Sci. 2021;10(1):158–66.
39. Yu H, Qiu Y, Pang X, et al. Lycorine promotes autophagy and apoptosis via TCRP1/Akt/mTOR Axis inactivation in human hepatocellular carcinoma. Mol Cancer Ther. 2017;16(12):2711–23.
40. Kuroda K, Kiya K, Matsuzaki S, et al. Altered actin dynamics is possibly implicated in the inhibition of mechanical stimulation-induced dermal fibroblast differentiation into myofibroblasts. Exp Dermatol. 2023;32(11):2012–22.
41. Zhang Y, Wang S, Yang Y, et al. Scarless wound healing programmed by core-shell microneedles. Nat Commun. 2023;14(1):3431.
42. Yang ZR, Suo H, Fan JW, et al. Endogenous stimuli-responsive separating microneedles to inhibit hypertrophic scar through remodeling the pathological microenvironment. Nat Commun. 2024;15(1):2038.

Publisher's note